Int J Adv Manuf Technol (2013) 69:1087–1095
DOI 10.1007/s00170-013-5102-y

ORIGINAL ARTICLE

Improving prediction accuracy of thermal analysis for weld-based additive manufacturing by calibrating input parameters using IR imaging

Xingwang Bai · Haiou Zhang · Guilan Wang

Received: 4 March 2013 / Accepted: 27 May 2013 / Published online: 12 June 2013

Abstract In experiments, it is usually difficult to accurately determine simulation input parameters such as heat source parameters, material properties at high temperature, etc. The uncertainty of such input parameters is responsible for the large error of thermal simulation for weld-based additive manufacturing. In this paper, a new approach is presented to calibrate uncertain input parameters. The approach is based on the solution of the inverse heat conduction problem of small-scale five-layer deposition and the application of the infrared (IR) imaging technique. The calibration of heat source parameters involves a multivariate optimization search using the pattern search method, whereas the calibration of the combined radiation and convection model includes a number of one-dimensional searches using the Fibonacci search method. Based on an in-depth analysis of IR images, thermal characteristics such as mean layer temperature and cooling rate are selected as the comparison results and included in cost functions. Lastly, the validity of the approach is demonstrated by a simulation case of 15-layer deposition with calibrated input parameters. The comparison between the simulated and experimental results verifies the improved prediction accuracy.

Keywords Weld-based additive manufacturing · Finite element analysis · IR imaging · Inverse analysis

1 Introduction

So far, it is still economically impractical to fabricate large components using laser-based additive manufacturing. However, weld-based additive manufacturing is particularly useful in the manufacture of medium to large components due to its capability to fabricate fully dense components with high productivity and at low cost [1, 2]. Thus, weld-based additive manufacturing has caught a widening interest in recent years.

The application of weld-based additive manufacturing is generally evaluated on its performances in terms of residual stress, deformation, microstructure, and mechanical properties of the deposited component. Currently, reasonable prediction in these aspects and optimization of process parameters can be realized by the coupled thermal–metallurgical–mechanical simulation. Klingbeil et al. [3] used the one-dimensional (1D) axisymmetrical and 2D generalized plane strain thermomechanical finite element models to analyze the constrained residual stress state in deposited layers. Mughal et al. [4] developed a three-dimensional (3D) finite element model to predict the residual stress-induced deformations in weld-based additive manufacturing. Particularly, they found that the main cause of deformations was thermal cycling during deposition. Zhao et al. [5, 6] conducted a 3D finite element thermal analysis and mechanical analysis of single-pass multilayer weld-based additive manufacturing. Thermal cycles measured by two thermal couples and residual stresses measured through the hole-drilling strain-gage method were used to validate the calculated results. It was reported that the deposition in reverse directions results in improved heat diffusion condition and lower stresses.

Numerical simulations provide a better understanding of the dynamic thermal, metallurgical, and mechanical behaviors during weld-base additive manufacturing. However, the prediction accuracy of current available simulation still remains at the level of qualitative agreement with experiments according to pertinent literature.

Since the thermal solution is the basis of the following metallurgical and mechanical calculations, thermal analysis is a major source of uncertainty in the thermal–metallurgical–

X. Bai · H. Zhang (✉) · G. Wang
State Key Laboratory of Digital Manufacturing Equipment and Technology, Huazhong University of Science and Technology, Wuhan 430074, China
e-mail: zholab@hust.edu.cn

mechanical simulation. As illustrated in Fig. 1, a thermal finite element analysis of weld-based additive manufacturing can be considered as a function **f**, with input **x** including parameters in terms of geometry, heat input, heat loss, and material properties. The output **y** is the temperature history solution with specific characteristics including melt pool size, mean layer temperature, temperature gradient, and thermal cycle. By virtue of the complexity of welding phenomenon, some input parameters are currently difficult to accurately determine in experiments. The parameters of heat source size are usually decided by experience [7]. The high-temperature behavior of the material is often simplified due to the lack of data about material properties at high temperature [8]. Because the emissivity of a given material varies with temperature and surface finish, how to choose the appropriate value of emissivity in simulation is still a hard task. Inaccuracy in such aspects leads to a high simulation error of thermal analysis. A feasible method of minimizing error is to validate the thermal solutions and calibrate input parameters based on the experimentally determined data. The so-called calibration is essentially the solving process of an inverse heat transfer problem, i.e., an inverse analysis.

Key issues for the inverse analysis include what physical data to obtain in experiments and how to construct cost function correspondingly. In the area of conventional welding simulation, where the calibrations of input parameters have become common practice, the end crater geometry, the cross-section parameters of weld pool (width and penetration), and the thermal cycle measured by thermal couple are commonly used to calibrate the heat source model [7, 9, 10]. However, the cross-section geometry of weld pool is immeasurable in weld-based additive manufacturing, and the deficiency of the thermal couple is that the crucial temperature data of the deposited component are unavailable. So, infrared (IR) imaging is a better option for temperature measurement for weld-based additive manufacturing. IR imaging can record the temperature distributions on the surface of both base plate and the deposited component with high resolution of time and space. In fact, IR imaging has already demonstrated its ability of in situ process observation and flaw detection in the process of electron beam-based additive manufacturing [11].

In this paper, a new approach of calibrating uncertain parameters is developed based on inverse analysis and IR imaging to increase prediction accuracy. The calibration process repeatedly performs trial calculations of a small-scale five-layer deposition. The calibration of heat source parameters involves a multivariate optimization search using pattern search method (PSM), whereas the calibration of the combined radiation and convection model includes a number of one-dimensional search using the Fibonacci search method (FSM). Based on in-depth analysis of IR images, thermal characteristics such as mean layer temperature and cooling rate are selected as the comparison results and included in cost functions. Finally, the approach is validated by a simulation case of 15-layer deposition with calibrated input parameters. The comparison between the simulated and experimental results shows that the prediction error of temperature history is <30 °C in the simulated case.

2 Experimental work

The weld-based additive manufacturing system used in the study is a combination of gas metal arc welding (GMAW) and numerical control (NC) machine. The location, orientation, and movement of the welding torch as well as process parameters are controlled by the NC machine. AWS ER70S-6 steel wire of 1.6 mm diameter was employed as the welding consumables. The shielding gas composition was pure argon.

As shown in Fig. 2, a single-pass multilayer structure was deposited on the side edge of base plates so that the temperature on the large face of the base plate could be recorded by

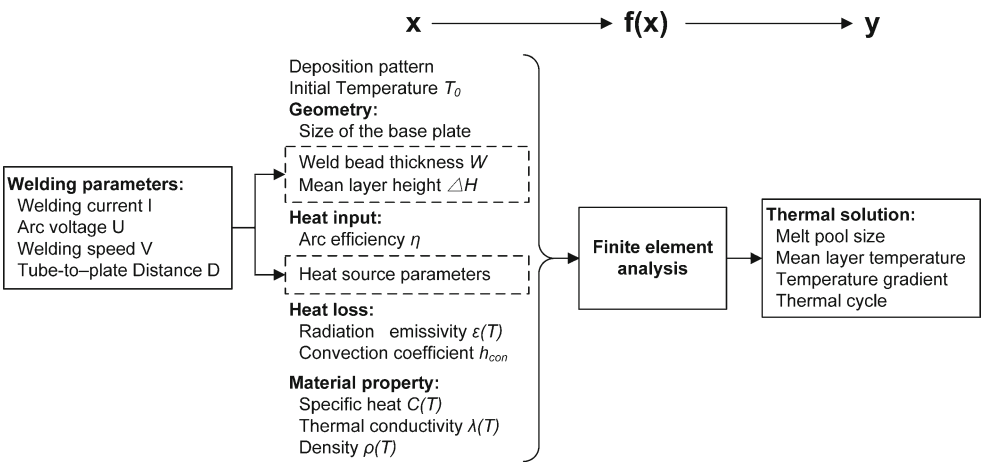

Fig. 1 Thermal analysis of weld-based additive manufacturing

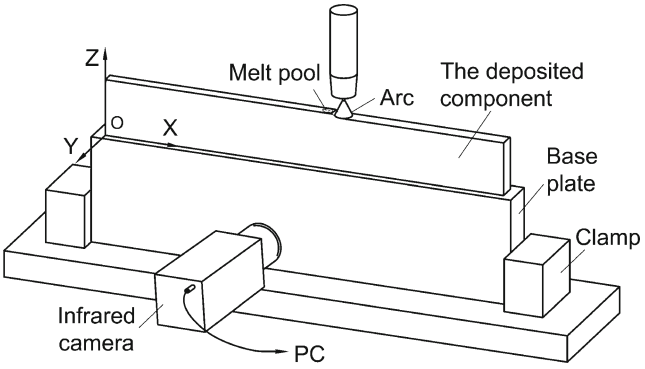

Fig. 2 Experimental setup

IR camera. The evolution of the temperature field was recorded using an IR camera FLIR ThermaCAM A320, which captured dynamical IR images of 320×240 resolution. The temperature data were treated using the software ThermaCAM Researcher.

Interlayer temperature control was carried out in experiments. The temperature at a selected point (located in the midline, 8 mm away from current top face) was chosen as reference temperature. After the deposition of a layer, the component was cooled in air until the reference temperature dropped to the threshold value, and then the deposition of the next layer started. Besides, the reverse deposition pattern was applied in the study. Adjacent layers were deposited along reverse directions.

3 Modeling and simulation procedure

3.1 Geometric model

The geometric model and finite element meshes are shown in Fig. 3. The x direction is the welding direction, namely, the longitudinal direction; the y direction is the through-thickness direction; and the z direction is the depositing direction, namely, the transversal direction. Both the deposited component and base plate are fully meshed with hexahedral elements for the five-layer trial calculation in the calibration. The element birth and death (activation and deactivation) technique is used to simulate material deposition. To realize the actual temperature history, the simulation strictly follows the time sequence of experimental deposition. Not only every layer of elements is activated in the same time sequence as in experiments, and there is idle time between consecutive layers and elements in a single layer are also activated according to the real-time sequence. Since each layer consists of at least one element in the depositing direction, the element length in depositing direction (EL_z) cannot be greater than the mean layer height (ΔH).

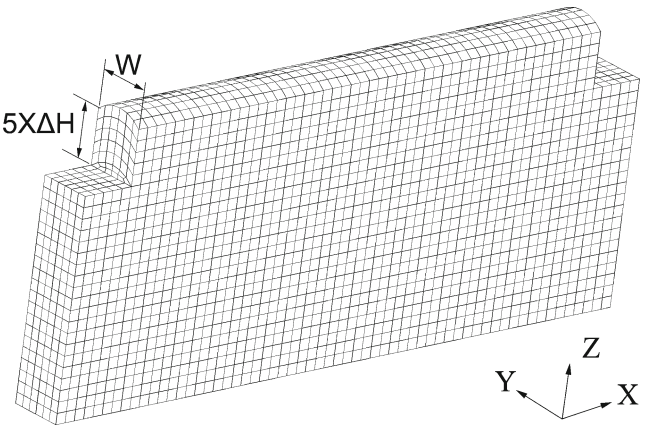

Fig. 3 Model and mesh generation

The two critical dimensions, thickness (W) and mean layer height (ΔH), can be determined in experiments, but a more systematic approach is to develop a mathematical model for the prediction of bead geometry according to input variables [12, 13]. Xiong et al. [14] presented a study of the application of a neural network and a second-order regression analysis for predicting bead geometry in weld-based additive manufacturing.

The prediction equation of the thickness as follows is employed in the study:

$$W = 8.9462 + 1.8088F - 0.3621V + 0.1739U - 0.5008D + 0.003556VD + 0.01667UD - 0.1169F^2 + 0.003137V^2 \quad (1)$$

where independent variables include wire feed rate F, welding speed V, arc voltage U, and nozzle-to-plate distance D. For most GMAW systems, weld current I is directly related with wire feed rate F.

Since the spatter rate is very low, it is acceptable to assume that the volume of metallic material remains constant after GMAW-based deposition. The mean layer height could be calculated as follows:

$$\Delta H = \frac{\frac{1}{4}\pi d^2 F}{VW} \quad (2)$$

where d is the wire diameter.

In addition, it is also important to establish a finite element model for the base plate according to the actual size. The size of the base plate is associated with heat diffusion condition.

3.2 Thermal models and material properties

An appropriate heat source model for the GMAW-based additive manufacturing procedure is the double ellipsoidal heat source model as demonstrated in reference [15]. Consisting of two different single ellipsoids, as shown in Fig. 4, the double ellipsoid heat source model has considerable flexibility in modeling realistic shapes of the asymmetrical moving heat sources. The heat density at an arbitrary point

(x, y, z) within each semi-ellipsoid is described by the following equations:

$$q_r(x,y,z,t) = \frac{6\sqrt{3} f_r \eta UI}{a_r bc\pi\sqrt{\pi}} e^{\frac{-3x^2}{a_r^2}} e^{\frac{-3y^2}{b^2}} e^{\frac{-3z^2}{c^2}} \quad x < 0 \tag{3}$$

$$q_f(x,y,z,t) = \frac{6\sqrt{3} f_f \eta UI}{a_f bc\pi\sqrt{\pi}} e^{\frac{-3x^2}{a_f^2}} e^{\frac{-3y^2}{b^2}} e^{\frac{-3z^2}{c^2}} \quad x \geq 0 \tag{4}$$

$$f_r + f_f = 2 \tag{5}$$

where q_r and q_f are the heat flux on the front and the rear semi-ellipsoid, respectively; η is the arc efficiency; U is the arc voltage; I is the welding current; a_f is the front ellipsoidal semi-axes length; a_r is the rear ellipsoidal semi-axes length; b is the half width; c is the depth; f_f is the fraction of heat deposited in the front; and f_r is the fraction of heat deposited in the rear.

Metallic material dissipates heat to ambient air through radiation and convection. Instead of modeling radiation and convection separately, a combined heat transfer coefficient, as used in [16], is calculated as follows:

$$h = \frac{\varepsilon\sigma\left(T^4 - T_{amb}^4\right)}{T - T_{amb}} + h_{con} \tag{6}$$

where h is the combined heat transfer coefficient; ε is the emissivity; σ is the Stefan–Boltzmann constant; h_{con} is the convection coefficient; T is the temperature variable; and T_{amb} is the ambient temperature. Temperature unit is in kelvin.

Temperature-dependent, homogeneous, and isotropic properties of the material are used in the simulation. The microstructure evolution needs to be included in the material modeling of ferritic steels since their properties can change greatly due to the phase transformations. The latent heat generated by phase transformations is taken into account by modifying the specific heat curve with the change of temperature, as performed in a previous study [17]. The thermal conductivities at temperatures above the melt point are manually increased to 10 times the original value to imitate the convection effect caused by the fluid flow in the weld pool [10].

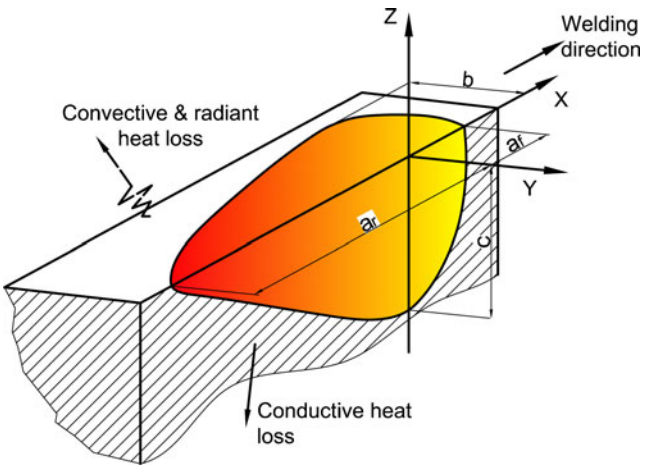

Fig. 4 Double ellipsoidal heat source model

4 Result and discussion

4.1 Mean layer temperature and the calibration of heat source parameters

Mean layer temperature T_{av} is defined as the average temperature of a rectangular area on the front surface 1 s after arc extinguishment of each layer deposition. The reason for choosing this instant is that a fully clear IR image cannot be acquired during deposition because of the light and smog interference from the arc. The T_{av} is designed to mainly reflect the aspect of arc heat input. As shown in Fig. 5, the top of the rectangular area AR1 is always aligned with the current top surface of the component. The size of AR1 is designed to be 60×10 mm. The choice of the AR1 size was found to have a negligible effect on the calibration results if AR1 is always large enough to cover the melt pool region regardless of the change of welding parameters.

Both experiment and simulation show that T_{av} increases with the increasing layer number, but the increment of T_{av} becomes very small after the third layer. This is attributed to the strict interlayer temperature control, which ensures that each layer of deposition starts at the same initial temperature. The T_{av} of the third, fourth, and fifth layers are selected as comparison results and used to calibrate heat source parameters.

Apparently, T_{av} is dependent on welding parameters. Experimental depositions are performed to obtain T_{av} corresponding to varied welding parameters. The IR-measured results of T_{av} are listed in Table 1. Welding

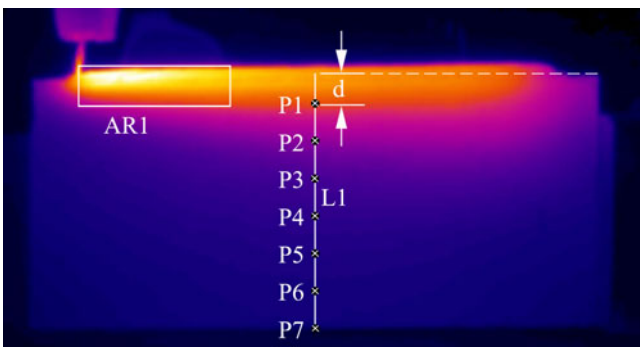

Fig. 5 The diagram of IR image treatment

Table 1 IR-measured results of the mean layer temperature T_{av}

F (m/min)	I (A)	V (cm/min)	U (V)	D (mm)	$T_{avm,3}$ (°C)	$T_{avm,4}$ (°C)	$T_{avm,5}$ (°C)
1.6	112	60	30	12	433.49	430.64	435.04
2.0	138	60	30	12	476.09	477.13	478.60
2.4	164	60	30	12	518.69	516.46	520.96
2.8	193	60	30	12	566.20	567.67	568.87
3.2	221	60	30	12	612.07	610.43	615.13
3.6	247	60	30	12	654.67	654.66	658.09
3.6	247	65	30	12	632.27	633.84	635.50
3.6	247	70	30	12	613.42	615.87	616.49
3.6	247	75	30	12	597.38	600.40	600.31
3.6	247	80	30	12	583.58	587.18	586.39
3.6	247	85	30	12	571.60	573.20	574.32
3.6	247	90	30	12	561.12	560.84	563.75

$T_{avm,i}$ indicates the IR-measured mean layer temperature of the ith layer

parameter configurations often used in the practice are chosen to be studied. In the practice of weld-based additive manufacturing, the layer geometry is controlled mainly through the adjustment of welding current and speed.

PSM is the optimization algorithm used for the calibration of heat source parameters. PSM is a family of numerical optimization methods that do not require the analytical expression or the gradient of the objective function to be optimized. Such direct search methods are suitable for the solution of the inverse problem in this research. A similar application of PSM can be found in the reference [7].

The heat source model as expressed in formulas 3 and 4 has seven input parameters of high uncertainty: η, a_r, a_f, b, c, f_r, and f_f. The PSM iteration will cost unbearably much time unless the calculation model is simplified. The heat distribution fractions f_f and f_r are supposed to be 0.45 and 1.55, respectively [16]. In the inverse analysis, η, a_r, and c are selected as the independent variables. Based on the observation of melt pool and arc using a high-speed camera, the following empirical expressions are used to constrain a_f and b:

$$a_r = 7a_f \tag{7}$$

$$b = 0.5W \tag{8}$$

Including the T_{av} of the third, fourth, and fifth layers, the error function for PSM analysis is designed as:

$$\mathrm{err} = \sqrt{0.3\left(\frac{T_{avs,3}-T_{avm,3}}{T_{avm,3}}\right)^2 + 0.3\left(\frac{T_{avs,4}-T_{avm,4}}{T_{avm,4}}\right)^2 + 0.4\left(\frac{T_{avs,5}-T_{avm,5}}{T_{avm,5}}\right)^2} \tag{9}$$

where $T_{avs,i}$ and $T_{avm,i}$ indicate the simulated and the IR-measured T_{av} of the ith layer.

The structure of the calculation procedure for the calibration of heat source parameters can be seen in Fig. 6. The first step is initialization. The geometric dimensions such as thickness W and mean layer height ΔH can be predicted by formulas 1 and 2 according to the welding parameters. The initial point $(\eta, a_r, c)_{(1)}$ can be selected by experience. The results of the previously finished calibrations can also provide reference for choosing initial point if welding parameters only have slight change. Choosing initial point near the optimum point can notably reduce iterations and save much computing time, as the PSM iteration comprising FEM analysis is time-consuming.

The results of the PSM solution are illustrated in Table 2. In view of the high computation cost, heat source parameters corresponding to only the variation of welding current and speed are estimated using PSM. PSM solution only includes the heat source parameters corresponding to the welding parameters that the experiment experienced. However, based on the PSM result, the nonlinear mapping between heat source parameters and welding parameters can be established through the method of regression or neural network. The combined use of these methods and finite element method can be found in references [7, 18].

4.2 Cooling rate and the calibration of radiation and convection model parameters

The thermal cycle at the arbitrary point on the surface of the component can be obtained based on the treatment of IR images at varying times. The thermal cycle curve describes the temperature variation with time. Key information of the thermal cycle curve includes peak temperature and cooling rate. If thermal cycle is expressed as a function with respect to time $T(t)$, the instantaneous cooling rate is the derivative of $T(t)$:

$$\tau(t) = \frac{\mathrm{d}T}{\mathrm{d}t} \tag{10}$$

Given that the base plate and the component are heat insulated from the fixture, the main factors affecting the

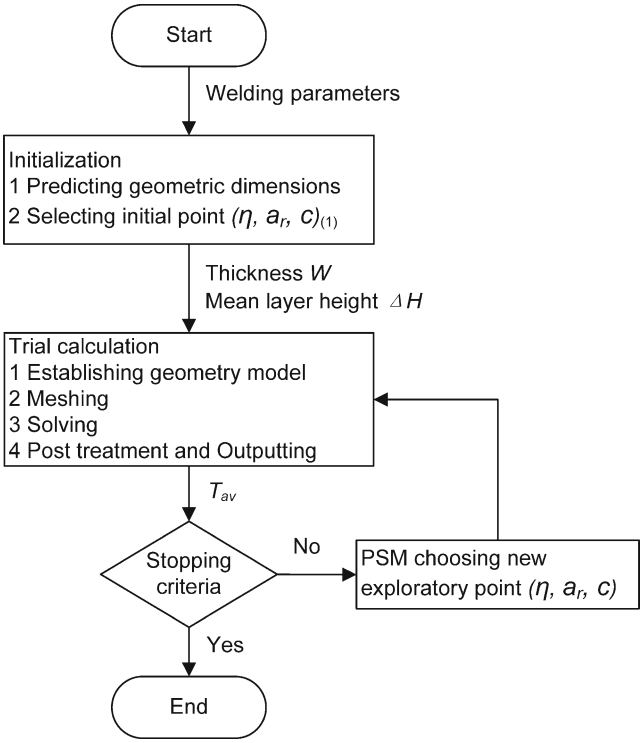

Fig. 6 The structure of the calculation procedure for the calibration of heat source parameters

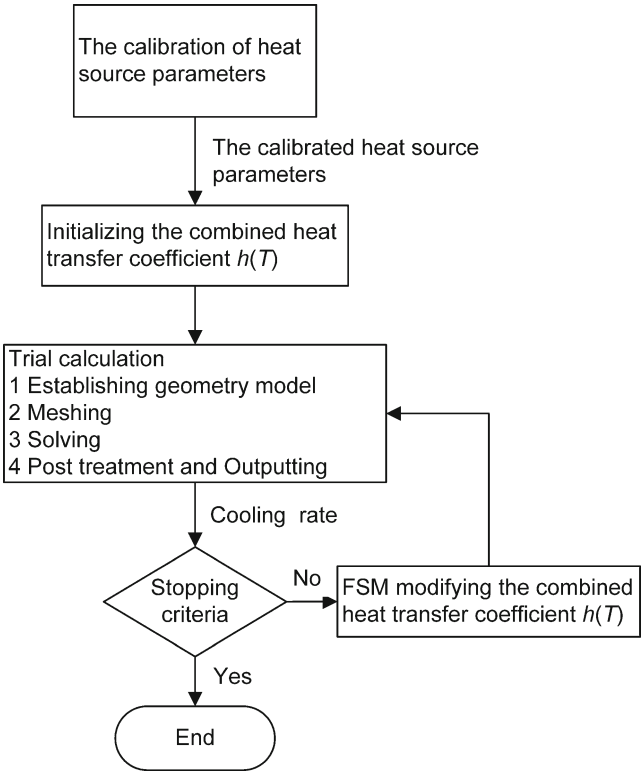

Fig. 7 The structure of the calculation procedure for the calibration of radiation and convection model parameters

cooling rate on the surface are radiation and convection. Thus, IR-measured cooling rate can be used to calibrate the radiation and convection model. According to formula 6, the combined heat transfer coefficient function has two independent variable ε and h_{con}. The emissivity ε is temperature dependent, $\varepsilon=\varepsilon(T)$, so formula 6 can also be expressed as:

$$h(T) = h_{\mathrm{rad}}(T) + h_{\mathrm{con}} \tag{11}$$

where h_{rad} is the contribution of radiation in the combined heat transfer coefficient.

In the programming, the temperature-dependent function $h(T)$ is defined by several data points with interpolation. The adjustment of the radiation and convection model is commonly realized by changing the data points:

$$\left\{h_{\mu_1}, h_{\mu_2}, h_{\mu_3}, \ldots, h_{\mu_n}\right\} \tag{12}$$

where h_{μ_i} is the combined heat transfer coefficient at temperature μ_i and n is the number of data points.

The criterion for the adjustment is based on the comparison between the IR-measured and simulated results of cooling

Table 2 The influence of welding current and speed on heat source parameters

F (m/min)	I (A)	V (cm/min)	U (V)	D (mm)	η (%)	a_{r} (mm)	c (mm)
1.6	112	60	30	12	88.516	31.599	6.506
2.0	138	60	30	12	87.260	32.231	6.471
2.4	164	60	30	12	85.783	32.457	6.627
2.8	193	60	30	12	84.564	33.635	6.865
3.2	221	60	30	12	83.434	34.359	6.945
3.6	247	60	30	12	82.283	35.228	7.031
3.6	247	65	30	12	80.587	35.743	6.847
3.6	247	70	30	12	82.066	37.362	6.507
3.6	247	75	30	12	83.456	36.245	6.265
3.6	247	80	30	12	81.744	36.764	6.064
3.6	247	85	30	12	81.447	37.465	5.903
3.6	247	90	30	12	83.279	37.612	5.632

rate. The thermal cycles at m points on the midline L1 are studied in the experiments and simulations. In the case shown in Fig. 5, the selected points are equal division points of the midline and m equals 7. Assuming that the cooling curves in a single thermal cycle are parallel to each other, the cooling rate at temperature μ_1, μ_2, μ_3, …, μ_n can be obtained by the following function in both simulation and experiment.

$$\tau_i = \frac{1}{m}\sum_{k=1}^{m}\frac{\mathrm{d}T_k}{\mathrm{d}t}\Big|_{T=\mu_i} \tag{13}$$

where τ_i is the cooling rate when the temperature is μ_i and T_k is the thermal cycle at the kth point.

The adjustment of the ith data point h_{μ_i} is decided by the error function shown in Eq. 14:

$$\mathrm{err}_i = \sqrt{\left(\tau_{i,S}-\tau_{i,M}\right)^2} \tag{14}$$

where $\tau_{i,S}$ and $\tau_{i,M}$ are the cooling rate at temperature u_i of the simulation and experiment results, respectively. If $\tau_{i,S}>\tau_{i,M}$, then the data point h_{μ_i} should be reduced; otherwise, the data point h_{μ_i} should be increased. The amplitude of adjustment is controlled by the FSM algorithm.

As illustrated in Fig. 7, the calibration of the combined heat coefficient was performed after the calibration of the heat source parameters, both with similar calculation procedures. The combined heat transfer coefficient is initialized using Eq. 6 with a constant emissivity of 0.8, convection coefficient of 10 W/(m^2 °C), and ambient temperature of 20 °C. Unlike the previous calibration, the inverse problem is solved by a number of concurrent one-dimensional searches rather than multidimensional search. FSM, one of the most efficient direct algorithms for one-dimensional search, is used in the calibration. FSM approaches the optimization location by means of successively narrowing the interval of uncertainty with the aid of Fibonacci numbers.

The initial and the resulting combined heat transfer coefficients in the calibration are compared in Fig. 8a. To demonstrate the extent of accuracy improvement after calibration, the thermal cycles at point P1 (as shown in Fig. 5,

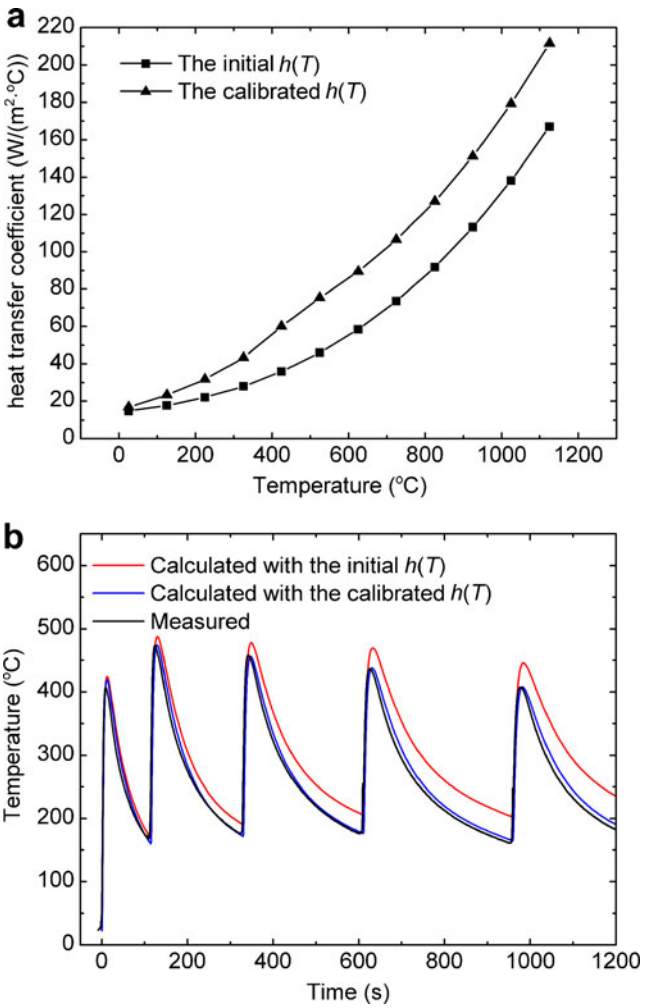

Fig. 8 Accuracy improvement after the calibration of the radiation and convection model

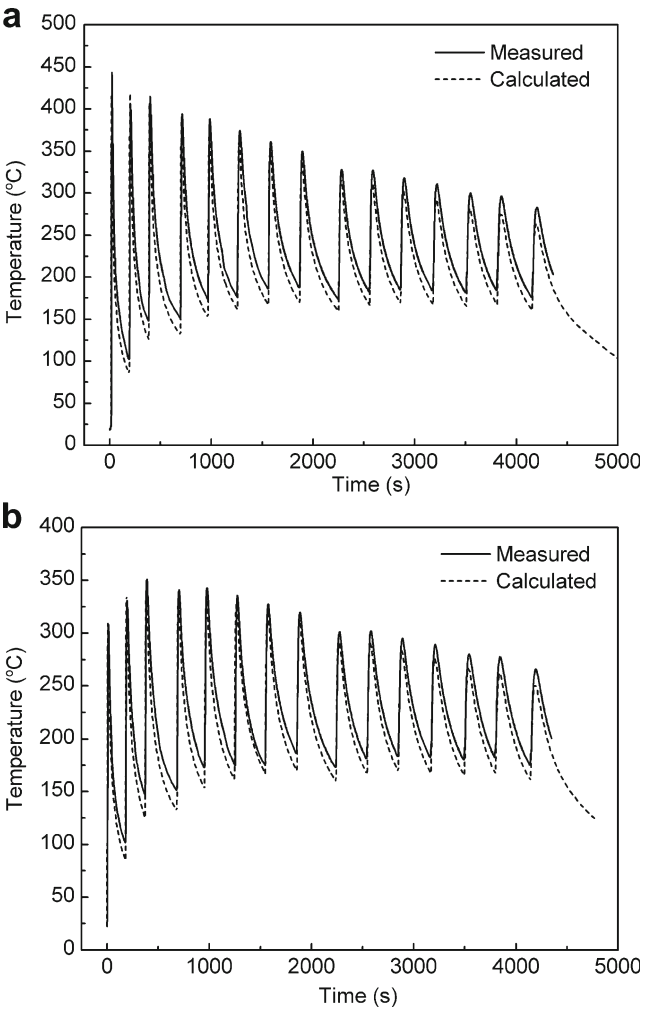

Fig. 9 Comparison of the measured and the calculated thermal cycles **a** at point A and **b** at point B

distance D=8 mm) produced by the initial and the resulting combined heat transfer coefficients are compared in Fig. 8b, certainly with the same welding parameters (I=247 A, V=60 cm/min, U=30 V, and D=12 mm).

4.3 Test case result

After calibration, testing simulations and experiments of 15-layer deposition are performed to verify that the prediction accuracy will be improved with the calibrated input parameters even in the case of more complex deposition. Figure 9 presents the thermal cycles at two points A and B measured by IR imaging in comparison to the calculated thermal cycle at a corresponding node position. Points A and B are in the mid-line, 5 and 10 mm below the top of the base plate, respectively. The thermal cycles show a good agreement both for peak temperature and cooling rate. The maximum errors occur around the troughs of the thermal cycle curves, all <30 °C. The large errors around troughs are due to the deviation of the convection coefficient. As known, natural convection is geometry dependent. The prediction accuracy is apparently improved compared with the published studies on weld-based additive manufacturing [4, 19].

The comparison of the calculated temperature field evolution with the measured result is another demonstration of prediction accuracy. Figure 10a–c depicts the measured temperature distributions 1 s after arc extinguishment in the 5th, 10th, and 15th layers, respectively, while Fig. 10d–f depicts the corresponding calculated temperature distribution in the 5th, 10th, and 15th layers, respectively. A good agreement can be found between the measured and the calculated temperature fields. The deviations of maximum temperature and the sizes of each temperature zone are attributed to two factors: weld beads slightly collapse at the start and end of each layer and measuring error rises at the interface between metal and air due to limited image resolution.

5 Conclusion

A new approach based on inverse analysis and the application of IR imaging is proposed to calibrate input parameters of thermal simulation for weld-based additive manufacturing, thereby improving prediction accuracy. Based on the previous discussions, the following conclusions can be obtained:

1. Compared with the thermal couple, IR imaging is more suitable for temperature monitoring and recording in weld-based additive manufacturing. Diversified treatment of the temporal and spatial variations of temperature acquired by IR imaging provides many experimental criteria by which it is feasible to calibrate all input parameters of thermal simulation.
2. The heat source parameters corresponding to varied welding parameters can be obtained through a multivariate search using the algorithm of PSM. Mean layer temperature which mainly reflects the arc heat input can be used to construct the cost function for the calibration.
3. A combined consideration of radiation and convection is much simpler than calibrating them separately. Cooling rate at a given temperature can be used to calibrate the combined heat transfer coefficient at the temperature; in

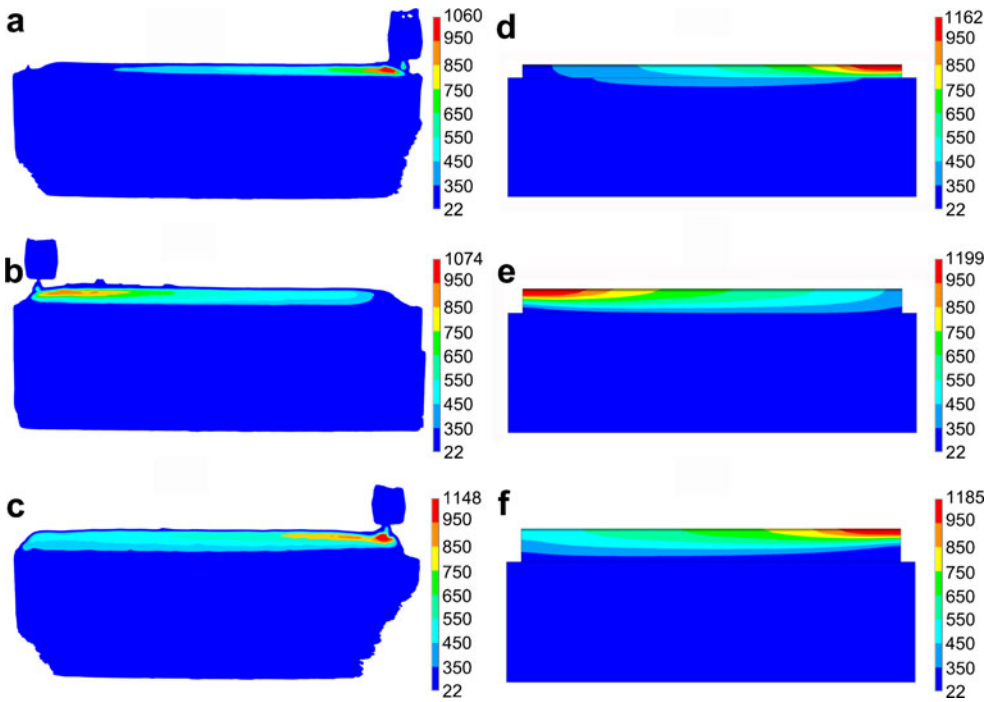

Fig. 10 **a**–**f** The temperature field evolution in weld-based additive manufacturing

this way, only a number of one-dimensional searches are needed in the calibration. The simplified inverse problem can be effectively solved by FSM.

4. The effect of calibration on prediction accuracy is examined by a test case. The comparison between the simulated and experimental results shows that the prediction error of temperature history is <30 °C in the test case. It could be expected that the proposed approach is also applicable to laser-based and electron beam-based additive manufacturing.

Acknowledgments This work was supported by the Natural Science Foundation of China (51175203). The authors would like to thank Yifeng Sun, Qi He, and Yun Pan for their experimental contributions.

References

1. Spencer JD, Dickens PM, Wykes CM (1998) Rapid prototyping of metal parts by three-dimensional welding. Proc Inst Mech Eng B J Eng Manuf 212(3):175–182
2. Wang F, Williams S, Rush M (2011) Morphology investigation on direct current pulsed gas tungsten arc welded additive layer manufactured Ti6Al4V alloy. Int J Adv Manuf Technol 57(5–8): 597–603
3. Klingbeil NW, Beuth JL, Chin RK, Amon CH (2002) Residual stress-induced warping in direct metal solid freeform fabrication. Int J Mech Sci 44(1):57–77
4. Mughal MP, Fawad H, Mufti RA (2006) Three-dimensional finite-element modelling of deformation in weld-based rapid prototyping. Proc Inst Mech Eng C J Mech Eng Sci 220(6):875–885
5. Zhao H, Zhang G, Yin Z, Wu L (2011) A 3D dynamic analysis of thermal behavior during single-pass multi-layer weld-based rapid prototyping. J Mater Process Technol 211(3):488–495
6. Zhao H, Zhang G, Yin Z, Wu L (2012) Three-dimensional finite element analysis of thermal stress in single-pass multi-layer weld-based rapid prototyping. J Mater Process Technol 212(1):276–285
7. Li P, Lu H (2011) Hybrid heat source model designing and parameter prediction on tandem submerged arc welding. Int J Adv Manuf Technol 62(5–8):577–585
8. Lindgren LE (2001) Finite element modeling and simulation of welding. Part 2: improved material modeling. J Therm Stress 24(3):195–231
9. Azar AS, Ås SK, Akselsen OM (2012) Determination of welding heat source parameters from actual bead shape. Comp Mater Sci 54:176–182
10. Heinze C, Schwenk C, Rethmeier M (2012) Effect of heat source configuration on the result quality of numerical calculation of welding-induced distortion. Simul Model Pract Theory 20(1):112–123
11. Schwerdtfeger J, Singer RF, Körner C (2012) In situ flaw detection by IR-imaging during electron beam melting. Rapid Prototyp J 18(4):259–263
12. Kannan T, Yoganandh J (2009) Effect of process parameters on clad bead geometry and its shape relationships of stainless steel claddings deposited by GMAW. Int J Adv Manuf Technol 47(9–12): 1083–1095
13. Rao PS, Gupta OP, Murty SSN, Rao ABK (2009) Effect of process parameters and mathematical model for the prediction of bead geometry in pulsed GMA welding. Int J Adv Manuf Technol 45(5–6): 496–505
14. Xiong J, Zhang G, Hu J, Wu L (2012) Bead geometry prediction for robotic GMAW-based rapid manufacturing through a neural network and a second-order regression analysis. J Intell Manuf. doi:10.1007/s10845-012-0682-1
15. Goldak J, Chakravarti A, Bibby M (1984) A new finite element model for welding heat sources. Metall Trans B 15B(6):299–305
16. Abid M, Siddique M (2005) Numerical simulation to study the effect of tack welds and root gap on welding deformations and residual stresses of a pipe-flange joint. Int J Press Vessel Pip 82(11): 860–871
17. Ferro P, Porzner H, Tiziani A, Bonollo F (2006) The influence of phase transformations on residual stresses induced by the welding process—3D and 2D numerical models. Model Simul Mater Sci Eng 14(2):117–136
18. Chamekh A, Bel Hadj Salah H, Hambli R (2008) Inverse technique identification of material parameters using finite element and neural network computation. Int J Adv Manuf Technol 44(1–2):173–179
19. Zhao HH, Zhang GJ, Yin ZQ, Wu L (2011) A 3D dynamic analysis of thermal behavior during single-pass multi-layer weld-based rapid prototyping. J Mater Process Technol 211(3):488–495